

# Site response analysis of liquefiable soil employing continuous wavelet transforms

D. CHAVAN\*, T.G. SITHARAM\* and P. ANBAZHAGAN\*

Propagation of the earthquake motion towards the ground surface alters both the acceleration and frequency content of the motion. Acceleration–time record and Fourier amplitude spectrum of the motion reveal changes in the acceleration and frequency content. However, Fourier amplitude spectrum fails to give frequency–time variation. Wavelet transforms overcome this difficulty. In the current study, site response analysis of a liquefiable soil domain has been investigated employing wavelet transforms. Three earthquake motions with distinct predominant frequencies are considered. It is revealed that the moment soil undergoes initial liquefaction, it causes a spike in the acceleration–time history. From the analysis, frequency of the spikes is found to be greater than the predominant frequency of the acceleration time history recorded at the ground surface. Interestingly, the spikes belong to the sharp tips of the shear stress–shear strain curve. Immediately after the spike, acceleration deamplification is observed. Post-liquefaction deamplification (filtering) of the frequency components is also observed.

**KEYWORDS:** acceleration; liquefaction; pore pressures

ICE Publishing: all rights reserved

## NOTATION

$a$	scale
$b$	translation
$C(a, b; f(t); \psi(t))$	continuous wavelet transform coefficient
$t$	time
$\psi$	transforming function
*	complex conjugate

## INTRODUCTION

It is a well-established fact that when earthquake motion travels from its source to the ground surface, its characteristics such as acceleration and frequency content get altered (Ishihara, 1996; Kramer, 1996). Conventionally, characteristics of the ground motion are determined from acceleration–time record and Fourier amplitude spectrum. Acceleration–time record gives information regarding the peak acceleration and duration of the ground motions. Fourier amplitude spectrum is employed to understand the frequency content of the ground motions. It provides detailed information about frequency components and the corresponding Fourier amplitudes. Higher Fourier amplitude implies that that particular frequency component exists for a longer period of time (Polikar, 1996). Furthermore, from Fourier amplitude, predominant frequency is obtained and compared with the natural frequency of the ground to observe if any possibility of resonance exists. It is worth noting that Fourier amplitude spectrum fails to give information regarding the time variation of the frequency (Kramer, 1996). This difficulty is overcome by

the use of wavelet transforms. Wavelet transforms provide the variation of frequency with time.

Liquefaction has been one of the major concerns in the field of geotechnical engineering (Ishihara, 1993; Idriss & Boulanger, 2008). It is broadly classified into (1) flow liquefaction and (2) cyclic mobility (Kramer, 1996). In flow liquefaction, soil mass undergoes extremely large deformations due to sliding of the liquefied mass. On the contrary, in cyclic mobility, the soil suffers from large but limited deformations due to alternate softening and hardening of the soil. Zeghal & Elgamal (1994) carried out analysis of liquefaction for recorded earthquake motions and found that post-liquefaction large shear strains resulted in hardening of the soil. Furthermore, post-liquefaction acceleration spikes were also noted. They attributed strain hardening and acceleration spikes to the large strain dilative tendency of the soil. Kokusho (2014) considered the cyclic mobility response observed in a cyclic triaxial test and investigated a base isolation effect considering liquefied layer overlying non-liquefied layer. Kokusho found that cyclic mobility reduced the base isolation effect to some extent. Gang *et al.* (2018) carried out analysis of liquefaction considering the cyclic mobility stress–strain response and found post-liquefaction high-frequency acceleration spikes in the ground surface response. Veeraraghavan *et al.* (2019) investigated the issue of high-frequency content at the ground surface modelling the stress–strain response of the soil by using a non-linear spring dashpot system. They concluded that if the pointed hysteretic stress–strain curve and/or non-elliptical stress–strain curve is a reality, then the presence of higher-frequency components in the output acceleration record is also a reality. The current study sheds further light on the evolution of spikes, frequency of spikes, correspondence between spikes and stress–strain response, employing time domain, frequency domain and joint time–frequency domain analysis. For joint time–frequency analysis, one-dimensional (1D) continuous wavelet transforms (CWTs) have been used.

Manuscript received 5 August 2021; accepted 6 December 2021.

\*Department of Civil Engineering, Indian Institute of Science, Bangalore, India.

## ABOUT 1D CWTS

Wavelet is a short duration wave that grows and decays fast (Chakraborty & Okaya, 1995; Polikar, 1996). Wavelet transforms employ wavelets to provide distribution of frequency with time for a non-stationary signal (Chakraborty & Okaya, 1995; Bonal *et al.*, 2012). A non-stationary signal is the one in which the frequency of the signal varies with time (Polikar, 1996). In the case of earthquake loading, the magnitude and frequency of the acceleration vary with time. Therefore, the acceleration–time record is also a non-stationary signal. The expression for a CWT is as follows (Polikar, 1996; MathWorks, 2021):

$$C(a, b; f(t); \psi(t)) = \int_{-\infty}^{\infty} f(t) \frac{1}{a} \psi^* \left( \frac{t-b}{a} \right) dt \quad (1)$$

where  $C(a, b; f(t); \psi(t))$  is a CWT coefficient,  $t$  is the time,  $a$  is the scale and  $b$  is the translation,  $\psi$  is a transforming function called as mother wavelet and  $*$  stands for complex conjugate. Mother wavelet is scaled and/or translated during the transformation. Scale either compresses or stretches the mother wavelet. Smaller scale means mother wavelet is compressed and larger scale means mother wavelet is stretched. Scale can be grossly looked at as inverse of the frequency. Thus, small scale captures high-frequency component of the signal and large scale captures low-frequency

components. Translation  $b$  defines the position of the scaled/original mother wavelet at particular time  $t$ .

## READING MAGNITUDE SCALOGRAM OF THE CWTS

The magnitude scalogram represents the distribution of the magnitude with time and frequency. Magnitude is the value of the CWT coefficient. Magnitude zero implies that particular frequency is absent in the signal at the specified time. Higher magnitude implies that that particular frequency is present at the specified time (Chatterjee, 2015). Figure 1(a) shows the artificially generated sinusoidal signal of frequency 10 Hz. Unit of amplitude is immaterial. The sampling frequency is 200 data points per s. Figure 1(b) shows the Fourier amplitude spectrum of the signal. It is clear from Fig. 1(b) that the predominant frequency of the signal is 10 Hz. The magnitude scalogram of the signal is shown in Fig. 1(c). Magnitude scalogram shows that the frequency of the signal is likely to be between 8 and 13 Hz. However, the magnitude is highest for the frequency component of 10 Hz. This implies that the frequency of the signal is 10 Hz.

Researchers such as Chakraborty & Okaya (1995) carried out frequency–time decomposition using CWTs. They opined that the use of wavelet transforms helps in improving

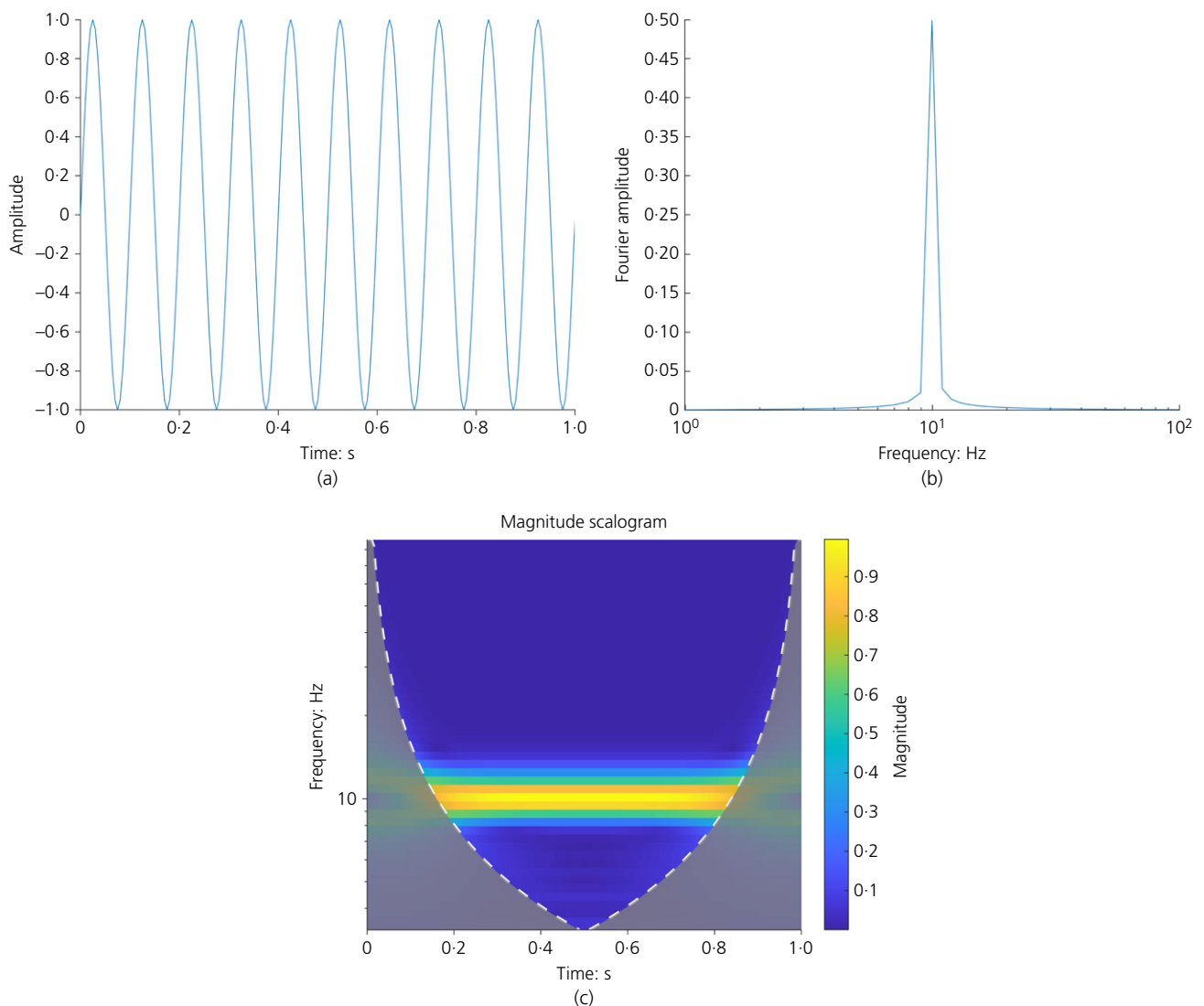


**Fig. 1.** Illustration of the wavelet scalogram: (a) sinusoidal signal, (b) Fourier amplitude spectrum, (c) wavelet scalogram

processing of seismic data. Baker (2007) employed wavelet transforms to extract pulse-like signals from a ground-motion time record and performed the quantitative classification of near-fault ground motions. Todorovska *et al.* (2009) used wavelet approximation for reduced representation of ground-motion records. They proposed that wavelet approximation could be effectively used in the synthesis of artificial ground-motion records. Kamgar *et al.* (2021) used discrete wavelet transforms in the non-linear seismic analysis of soil–structure interaction problems. Javdanian *et al.* (2021) used wavelet transforms along with the denoising and downsampling method to decompose the ground-motion records. They found that the site response under the main earthquake record was in close agreement with that from the wavelet-based record.

It should be noted that the wavelet transform adopted in the current study is a 1D CWT. The wavelet transforms in the current study are obtained by writing a code in MATLAB (R2020a) (MathWorks, 2020).

## DISCRETISATION OF THE GROUND

In the current study, horizontal ground with a thickness of 30 m is considered. The relative density and the degree of saturation of the ground are assumed to be 40 and 100%, respectively. The domain is discretised into four-node bilinear isoparametric plane strain quadUP elements. The vertical dimension of the element is 0.5 m, and the horizontal dimension is 1 m. This element has the capability to simulate the coupled solid-fluid response under dynamic loading. The vertical dimension is arrived at from the Kuhlemeyer & Lysmer (1973) criterion. Bedrock with a mass density of  $2.5 \text{ t/m}^3$  and shear wave velocity of 700 m/s is assumed to be at a depth of 30 m as per Anbazhagan *et al.* (2016). The earthquake load is applied at the base of the model in the form of equivalent nodal shear force (Joyner & Chen, 1975). Further details about the quadUP element and boundary conditions are shown in Fig. 2. It should be noted that the modelling approach adopted here simulates the vertically propagating horizontal shear wave (Pietruszczak *et al.*, 2003).

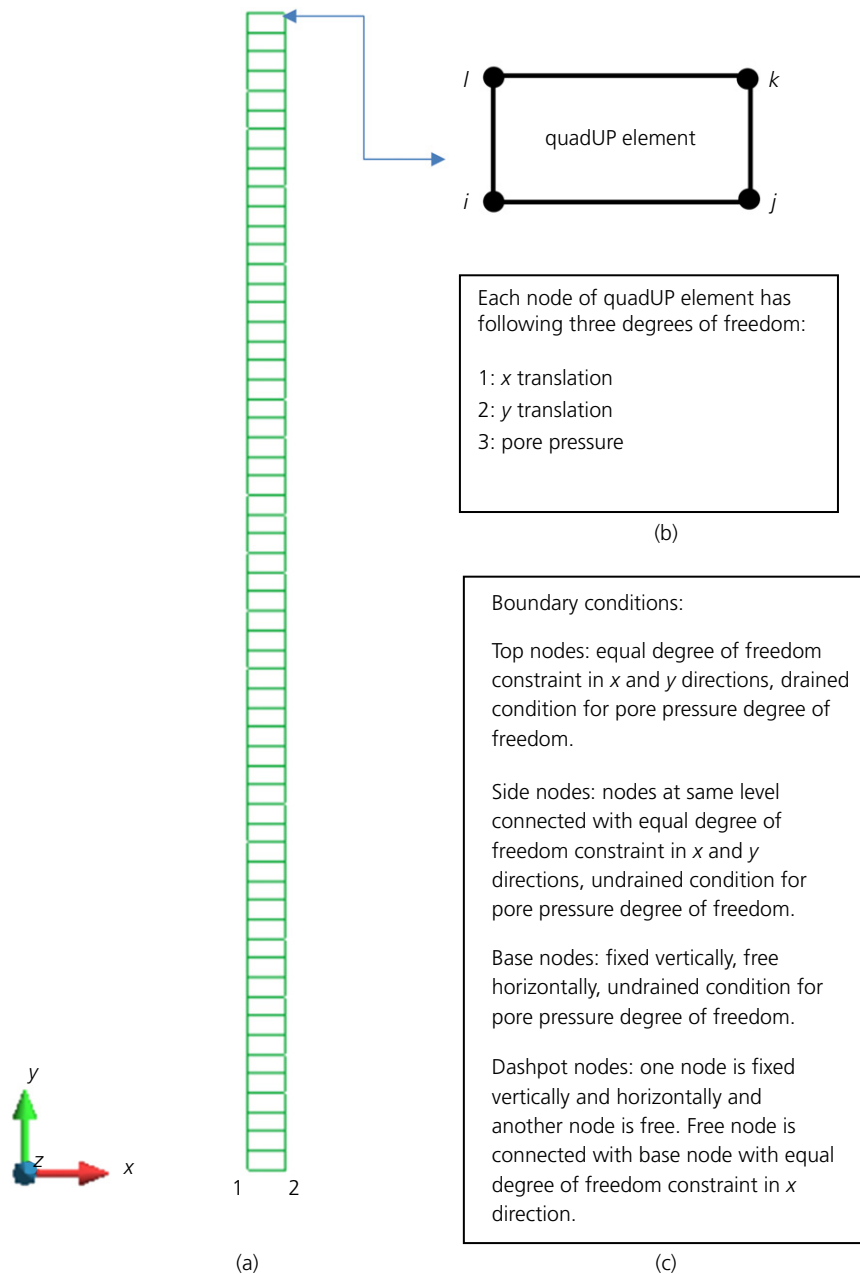


**Fig. 2.** Details of soil column discretisation: (a) finite-element mesh, (b) quadUP element, (c) details of boundary conditions

### Evaluation of the constitutive parameters

The constitutive model used in the current study is a pressure-dependent multi-yield material model named 'PressureDependMultiYield' in OpenSees (Mazzoni *et al.*, 2007). The model can be used in plane strain and three-dimensional problems. The constitutive formulation of the model is based on the framework of multi-surface plasticity. It uses a Drucker–Prager yield criterion. The model simulates the shear-induced volume contraction and dilation – that is, dilatancy and cyclic mobility observed for sandy soil under general loading conditions. To date, the literature mentions several soil models that can capture the hysteretic response of the saturated sandy soil under cyclic loading, but very few of them are capable of capturing a typical cyclic mobility response observed during undrained cyclic loading of saturated medium–dense sand. The model captures not only the hysteric response, but also typical cyclic mobility (Elgamal *et al.*, 2002, 2003). When used with regular solid elements, this model simulates the drained response. On the contrary, when used with solid-fluid fully coupled elements, it simulates an undrained response. Furthermore, the partially drained response can

also be simulated by defining a relatively large value of permeability.

The model has a total of 15 constitutive parameters. These parameters are mainly divided into the following three categories (Yang, 2000):

- Yield surface parameters*: parameters that define the size of yield surface such as small strain shear modulus and bulk modulus at reference effective confining mean pressure, peak friction angle, reference effective mean confining pressure and pressure-dependency coefficient. In the current study, small strain moduli are obtained from the expression suggested by Seed & Idriss (1970). A peak friction angle has been computed from the critical state friction angle by following the procedure recommended by Bolton (1986). Peak shear strain (0.1), reference effective mean confining pressure (80 kPa) and pressure-dependency coefficient (0.5) are taken from the values recommended in the OpenSees manual.
- Dilatancy parameters*: parameters controlling shear-volume coupling such as phase transformation

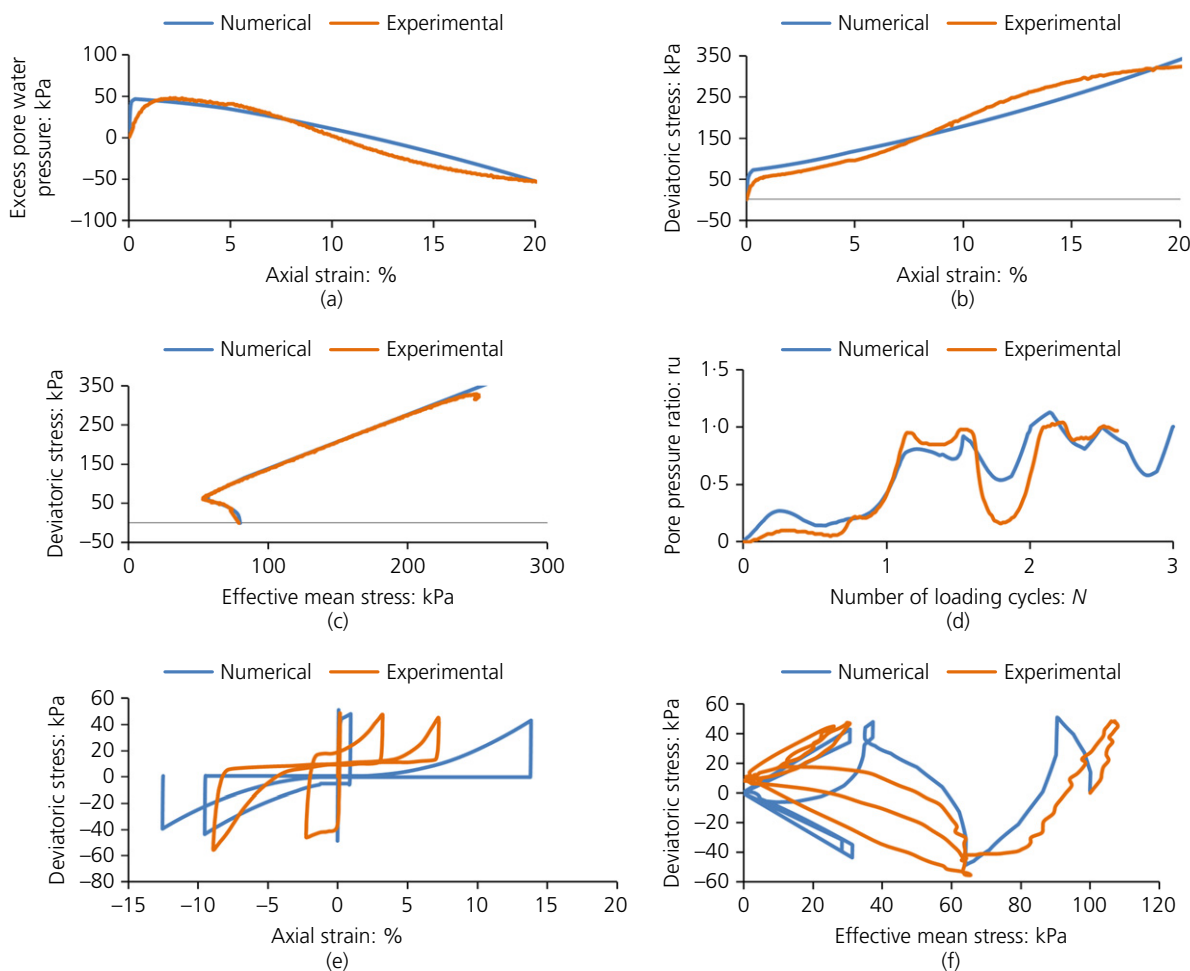


**Fig. 3.** Evaluation of the constitutive parameters: response for the monotonic test (a–c) and response for the cyclic test (d–f)

**Table 1.** Index properties of the fine clean sand used in the current study

Specific gravity ( $g$ )	$e_{\max}$	$e_{\min}$	$\rho_{\max}$ : $g/cm^3$	$\rho_{\min}$ : $g/cm^3$	$D_{10}$ : mm	$D_{30}$ : mm	$D_{50}$ : mm	$D_{60}$ : mm	$C_u$	$C_c$
2.65	0.84	0.45	1.83	1.44	0.14	0.20	0.27	0.30	2.14	0.95

angle, contraction and dilation parameters. The dilatancy is captured by using the following parameters: *contrac*, *dilat1* and *dilat2*. The parameter *contrac* is a non-negative constant that defines the rate of decrease in shear-induced volume in drained loading and the rate of pore pressure build-up in undrained loading.

Larger is the value, faster is the generation of pore pressure. Parameters *dilat1* and *dilat2* are non-negative constants that define the rate of increase in shear-induced volume in drained loading and the rate of decrease in pore pressure in undrained loading due to dilative tendency. The larger value of these two parameters stands for faster reduction in the pore pressure. The phase transformation angle is obtained from the isotropically consolidated undrained compression tests conducted in the current study. Dilatancy parameters are obtained by matching experimental results obtained from isotropically consolidated undrained compression triaxial tests with numerical ones as shown in Figs. 3(a)–3(c).

- (c) *Cyclic mobility parameters*: these parameters define the onset and evolution of cyclic mobility response. There are total of three such parameters: *liquefac1*, *liquefac2* and *liquefac3*. The parameter *liquefac1* defines the effective confining pressure below which the cyclic mobility mechanism is in effect. The parameter *liquefac2* defines the maximum amount of perfectly plastic shear strain developed at zero effective confinement during each loading phase. The parameter *liquefac3* defines the maximum amount of biased perfectly plastic shear strain accumulated at each loading phase under biased shear loading conditions. These parameters are obtained by matching the numerical response with that obtained from isotropically consolidated undrained cyclic triaxial tests as shown in Figs. 3(d)–3(f).

The values of constitutive parameters are: (1) saturated unit weight = 1.98 (t/m<sup>3</sup>), (2) small strain shear modulus  $G_{max}$  (kPa) at reference effective mean confining pressure of 80 kPa =  $7.83 \times 10^4$ , (3) small strain shear modulus  $B$  (kPa) at reference effective mean confining pressure of

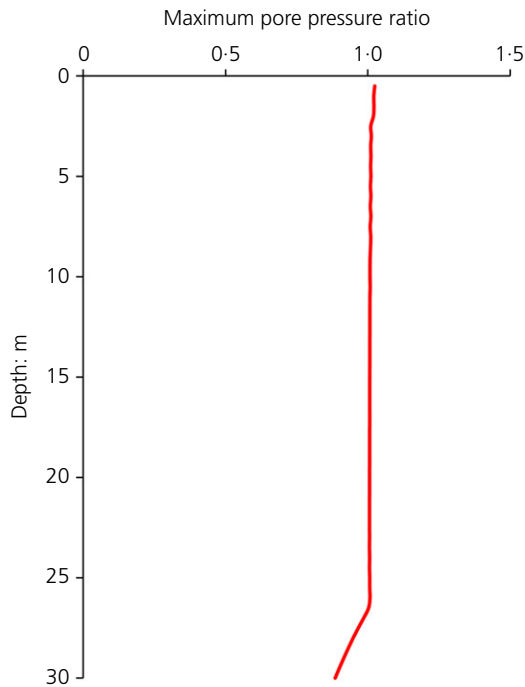


Fig. 4. Maximum pore pressure ratio profile along depth, input motion Bhuj 2001 earthquake

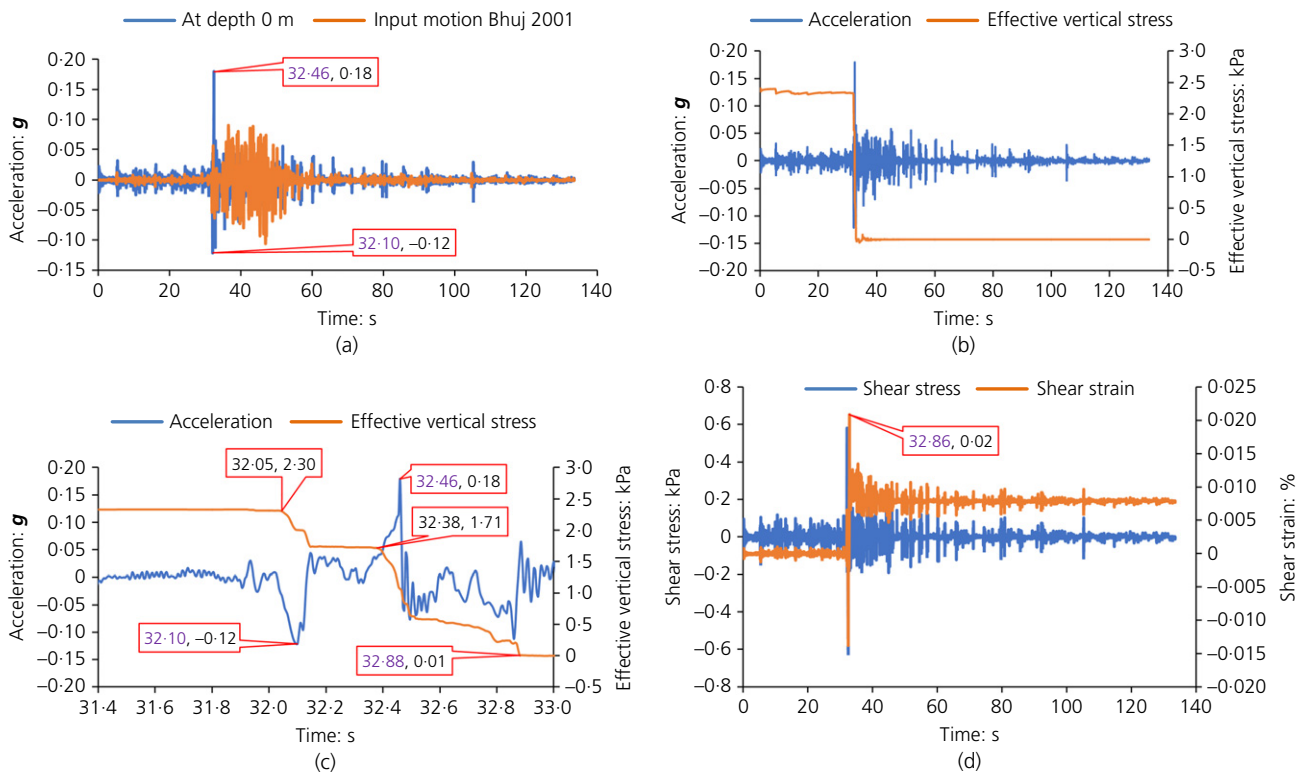
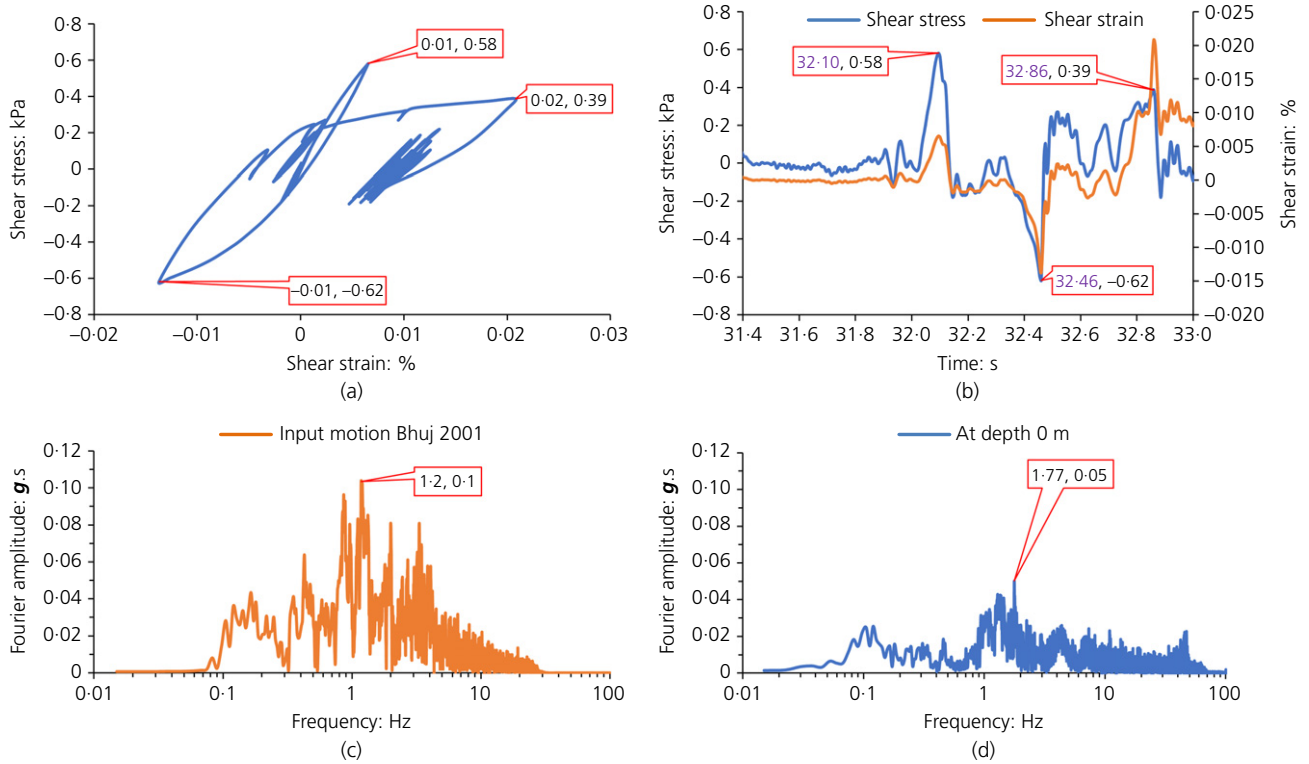


Fig. 5. (a) Acceleration records, (b) evolution of horizontal acceleration and effective vertical stress, (c) zoomed in view of the evolution of horizontal acceleration and effective vertical stress, (d) evolution of shear stress and shear strain, input motion Bhuj 2001 earthquake

80 kPa =  $1.98 \times 10^5$ , (4) friction angle ( $^\circ$ ) = 34.14, (5) phase transformation angle ( $^\circ$ ) = 26.56, (6) peak shear strain = 0.1, (7) reference effective mean confining pressure (kPa) = 80 kPa, (8) pressDependCoe = 0.5, (9) contrac = 0.4, (10) dilat1 = 0.01, (11) dilat2 = 0.2, (12) liquefac1 (kPa) = 10, (13) liquefac2 = 0.02, (14) liquefac3 = 1 and (15) Initial void ratio ( $e$ ) = 0.684. The monotonic and cyclic triaxial tests were conducted on a poorly graded fine clean

sand with a relative density of 40% having index properties given in Table 1.

Further details about the constitutive parameters and evaluation can be found in Chavan (2021). The coefficient of permeability of the soil obtained from the laboratory study was found to be  $3.36 \times 10^{-5}$  m/s, and the same was used in the analysis. The water table is assumed to be at the ground surface.



**Fig. 6.** (a) Shear stress–shear strain curve, (b) zoomed in evolution of shear stress and shear strain, (c) Fourier amplitude spectrum of input motion Bhuj 2001 earthquake, (d) Fourier amplitude spectrum of horizontal acceleration obtained at the ground surface in the present analysis, input motion Bhuj 2001 earthquake

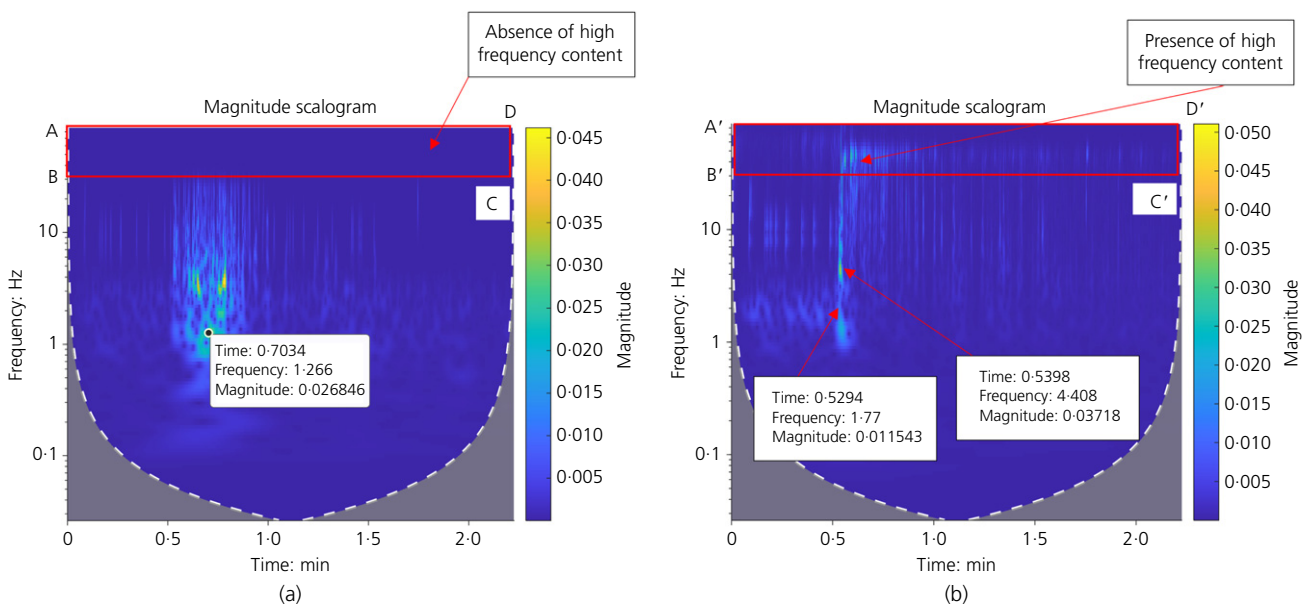


**Fig. 7.** Magnitude scalogram of the wavelet transform for (a) input motion Bhuj 2001 (b) of horizontal acceleration obtained at the ground surface in the current analysis

**Analysis stages**

Analysis was carried out in the following three stages: (1) gravity-elastic, (2) gravity-plastic and (3) dynamic-elastic plastic.

**INSIGHT INTO THE SEISMIC RESPONSE OF THE SOIL DOMAIN: BHUJ 2001 EARTHQUAKE**

Bhuj 2001, N78E component, recorded at Ahmadabad station, is used as input motion in the current analysis. Its magnitude is 7.0 (ML) and duration is 133.525 s. The peak

acceleration of this motion is 0.106 g, and it occurred at 46.94 s. The maximum pore pressure ratio profile along the depth during shaking is shown in Fig. 4. Pore pressure ratio is the ratio of excess pore water pressure and initial effective vertical stress at a given depth. From this figure, it is observed that the maximum pore pressure ratio is equal to 1 for soil mass above the depth of 26 m. This implies that soil over this region became liquefied during shaking.

The acceleration-time record obtained at the ground surface from the current analysis is shown in Fig. 5(a) along with input motion. It is observed that acceleration at the

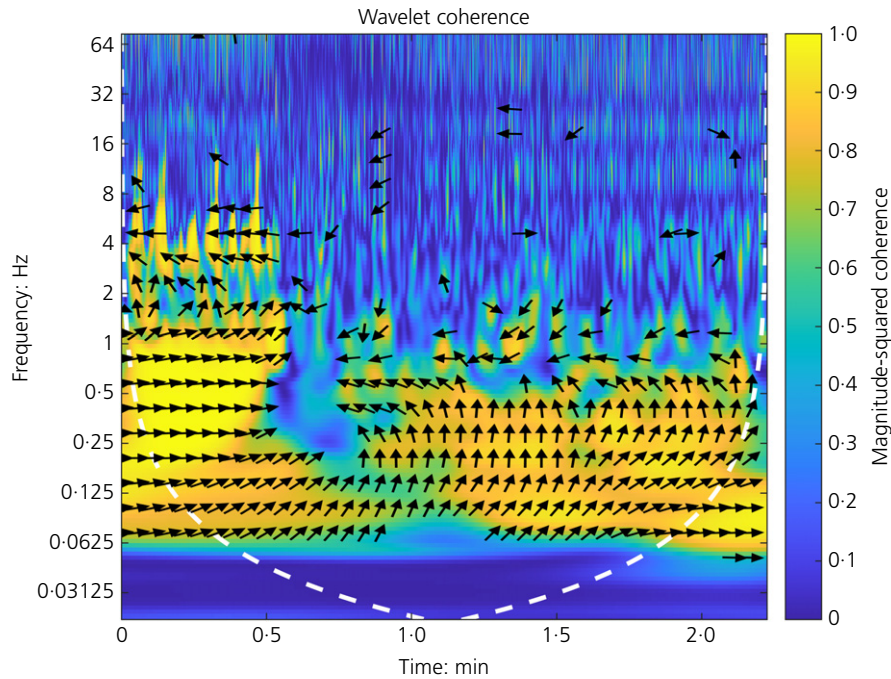


**Fig. 8.** Wavelet coherence between the Bhuj 2001 earthquake record and the corresponding acceleration record at the ground surface

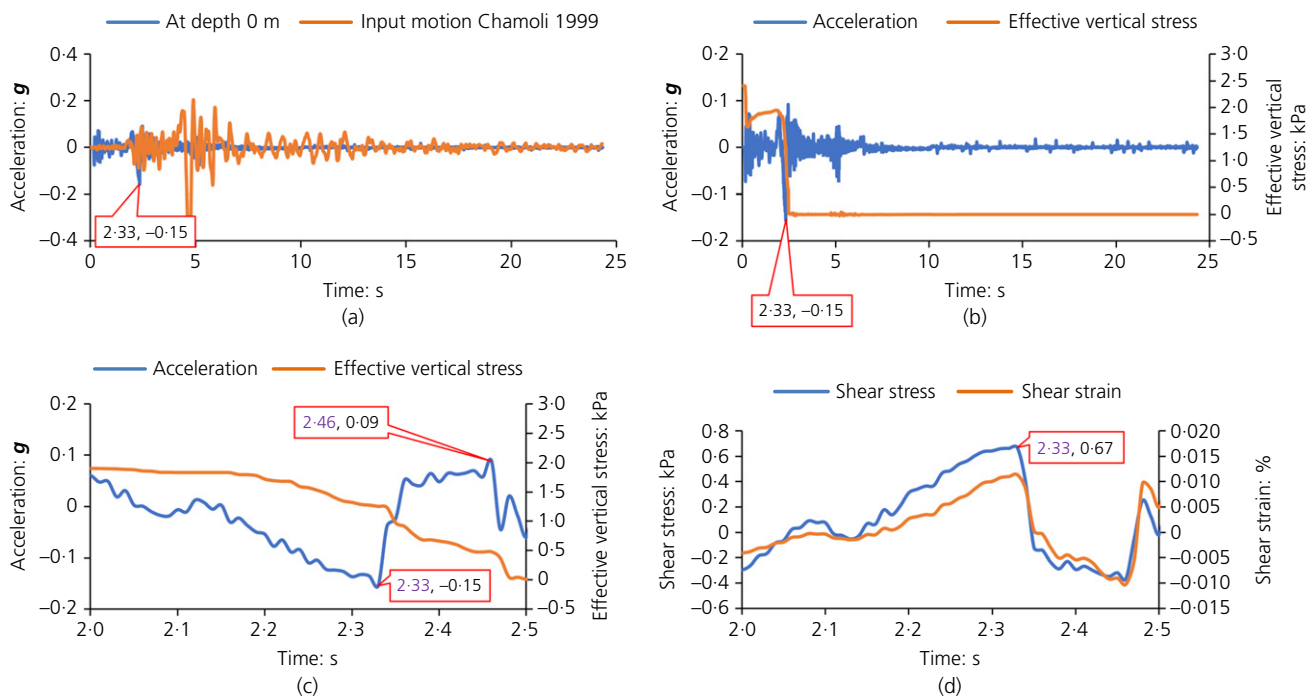


**Fig. 9.** (a) Acceleration records, (b) evolution of horizontal acceleration and effective vertical stress, (c) zoomed in view of evolution of horizontal acceleration and effective vertical stress, (d) evolution of shear stress and shear strain for the Chamoli earthquake (1999)

ground surface – that is, depth of 0 m, increases suddenly and sharply at around 32 s. Furthermore, immediately after the spike, acceleration deamplification is observed. This means that acceleration in the ground surface record is less than its counterpart in the input motion. To investigate why this sudden spike occurs in the acceleration, acceleration and effective stress evolution are plotted together in Figs. 5(b) and 5(c). It should be noted that effective vertical stress shown in Figs. 5(b) and 5(c) is at a depth of 0.25 m. This is so because in finite-element analysis, stresses and strains are computed at the integration points (Gauss points). The quadUP element has Gauss points at the mid of the sides. Furthermore, effective vertical stress is the total vertical stress minus pore water pressure. From Fig. 5(b), it is observed that there is a sudden drop in the effective stress at around 32 s, and this could be probably the cause of the spike in the ground surface acceleration. To investigate this issue further, acceleration and effective stress are zoomed in from 31.4 to 33 s, as shown in Fig. 5(c). It should be noted that effective vertical stress considered here is computed at the Gauss point at a depth of 0.25 m, and acceleration is recorded at the topmost node. From this figure, it is clear that when there is a sudden drop in the effective stress, there is a sudden rise in the acceleration, and when the effective

stress is constant, the corresponding acceleration is also almost constant. It should be noted here that a change in the effective stress changes the stiffness of the soil. When there is a reduction in the stiffness, soil undergoes large straining. This argument is supported by the shear strain evolution shown in Fig. 5(d). A drop in the effective stress results in a sudden and relatively large shear straining at around 32 s as observed in Fig. 5(d). This increase in the shear strain is accompanied by an increase in shear stress as shown in Fig. 5(d). Thus, a drop in the effective stress results in an acceleration spike (acceleration amplification) that is mainly due to a sudden rise in the shear stress, which is accompanied by a sudden rise in shear strain.

From the shear stress–shear strain curve shown in Fig. 6(a) and shear stress, shear strain evolution shown in Fig. 6(b), it is clear that the acceleration spike corresponds to the tip of the stress–strain curve. This is so because, at the tip of the stress–strain curve, there is a sudden change in the stiffness of the soil. Observing Figs. 5(c), 6(a) and 6(b) together, the above point is justified. Furthermore, the Fourier spectrum for input motion and acceleration record obtained from the current study at the ground surface (at 0 m depth) is shown in Figs. 6(c) and 6(d), respectively. These figures show that the predominant frequency of input

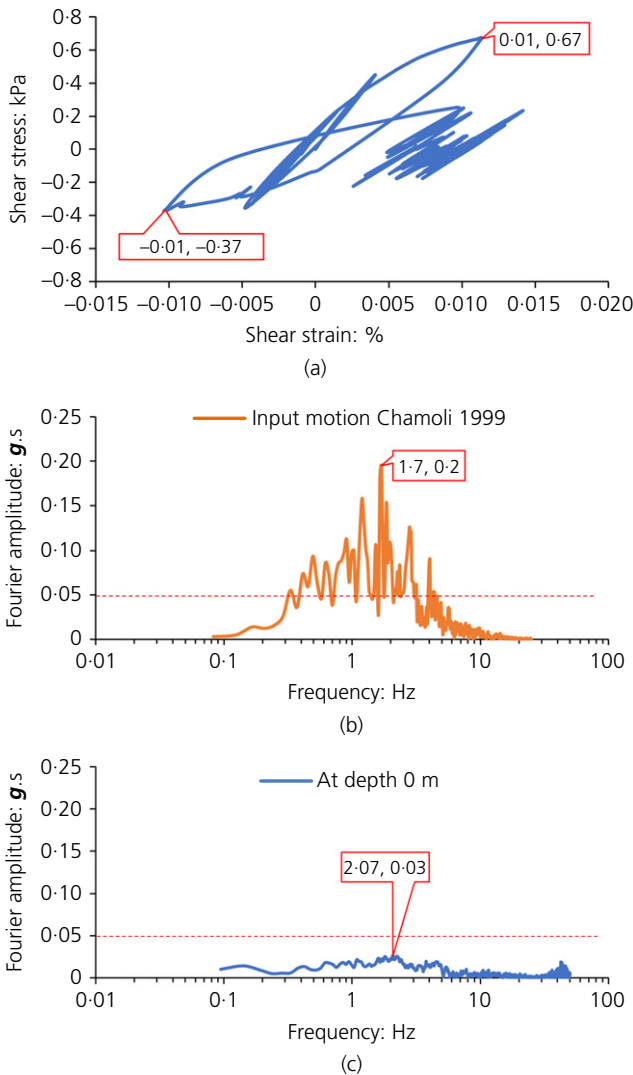


**Fig. 10.** (a) Shear stress–shear strain curve, (b) Fourier amplitude spectrum of input motion, (c) Fourier amplitude spectrum of horizontal acceleration obtained at the ground surface in the current analysis for the Chamoli earthquake (1999)

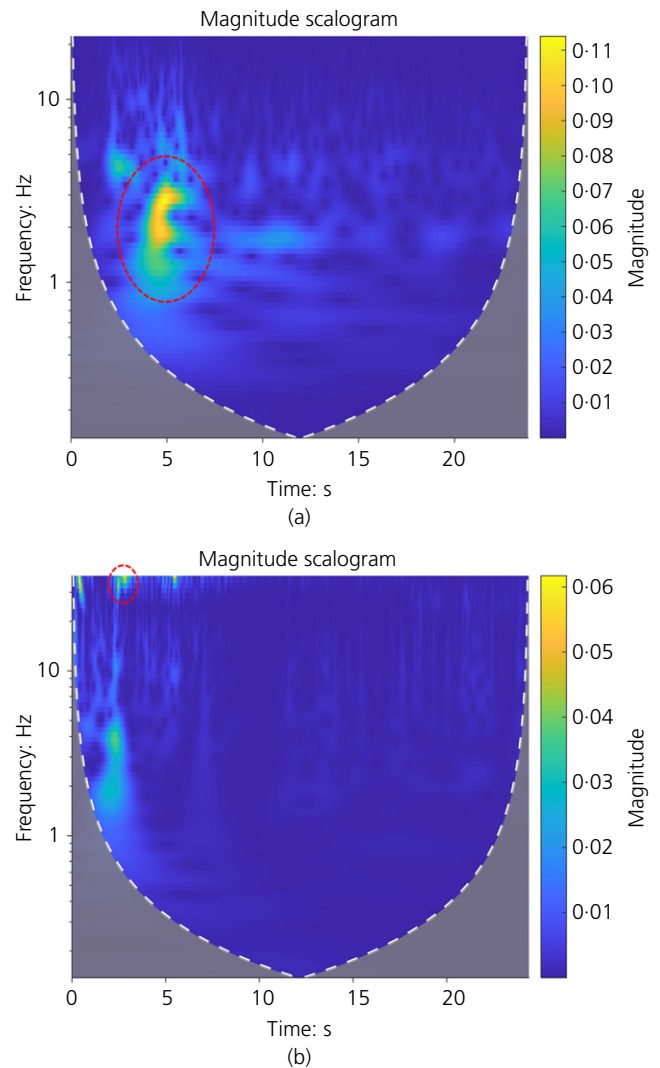


**Fig. 11.** Magnitude scalogram of the wavelet transform for (a) input motion Chamoli 1999 (b) of horizontal acceleration obtained at the ground surface in the present analysis for input motion Chamoli 1999

motion is 1.2 Hz whereas that of the acceleration record obtained from the current study is 1.77 Hz. The magnitude scalogram of the wavelet transforms for the input motion and acceleration record obtained at the ground surface from the current study are shown in Fig. 7. From this figure, it is found that the predominant frequency for the input motion occurs at around 42.2 s (i.e.  $0.7034 \times 60$ ) and that for acceleration obtained at the ground surface occurs at around 31.76 s (i.e.  $0.5294 \times 60$ ), respectively. Furthermore, the frequency of the acceleration spike belonging to the sudden drop in effective stress is 4.40 Hz.

From the Fourier amplitude spectrum and wavelet transform (region ABCD of wavelet transform) of input motion, it is observed that high-frequency components ( $>30$  Hz) are absent throughout the shaking. However, from the Fourier amplitude spectrum and wavelet transform of the surface motion, it is observed that post-liquefaction, high-frequency components ( $>30$  Hz) exist throughout the shaking. The post-liquefaction (i.e. after 32 s) spikes observed in the acceleration-time record are the high-frequency components. This finding is justified by wavelet transforms. In wavelet transforms, intermittent sharp light blue lines, over region A'B'C'D', present for the frequency above 30 Hz implies the presence of high-frequency components. The post-liquefaction high-frequency components might be due to the dilative tendency of the soil. However, the Fourier amplitude spectrum of the acceleration record at the ground surface obtained in the current analysis shows that high-frequency components in the range of 30–70 Hz are also present in the acceleration record. The bright shades in Fig. 7(b) belong to the high-frequency content. A comparison of the Fourier amplitude spectrum shows that the Fourier amplitude of the frequency components in the acceleration record obtained at the ground surface is significantly less than those in the input motion for frequencies up to 10 Hz. From 10 to 20 Hz, Fourier amplitude for both motions is almost the same.

Wavelet coherence between the Bhuj 2001 earthquake record (first signal) and acceleration-time record (second signal) at the ground surface from the current analysis is shown in Fig. 8. For frequencies above 4 Hz, no coherence exists between the two signals. Coherence exists for frequencies between 0.0625 and 4 Hz (mostly below 1 Hz). Arrows pointing to the right implies that signals are in phase – that is, signals move in the same direction; arrows pointing to the left means that signals are in anti-phase – that is, signals move in the opposite direction. Arrows pointing straight up implies that the first signal leads the second signal by  $90^\circ$ . The straight down arrow means that the first signal lags the second signal by  $90^\circ$ . As observed in Fig. 8, two signals are in phase for the frequency range of 0.2–0.75 Hz over a time span of 0–27 s (i.e.  $0.45 \times 60$ ). Very low coherence is observed for a time span between 30 (0.5 min) and 60 s (1 min). From 60 s, the onward first signal is observed to be leading the second signal.

INSIGHT INTO THE SEISMIC RESPONSES OF THE SOIL DOMAIN FOR CHAMOLI (1999) AND UTTARKASHI (1991) EARTHQUAKES

Additional simulations were carried out for Chamoli 1999 earthquake (station: Gopeshwar N20E, magnitude: 6.6 ms, PGA: 0.36g, duration: 24.32 s) and Uttarkashi 1991 earthquake (station: Bhatwari N85E, magnitude: 7.0 ms, PGA: 0.252g, duration: 36.14 s). Plots for acceleration and effective stress evolution for Chamoli 1999 earthquake are shown in Fig. 9. From Figs. 9(a) and 9(b), it is observed that a significant part of the input motion becomes deamplified after reaching a state of zero effective stress – that is, at time 2.33 s. The zoomed part of the acceleration and effective stress evolution shown in Fig. 9(c) reveals that a sudden reduction in the effective stress at 2.33 and 2.46 s gives rise to the corresponding spike in the acceleration. From Figs. 9(d) and 10(a), it is clear that the acceleration spike belongs to the tip of the shear stress-shear strain curve. From Figs. 10(b)

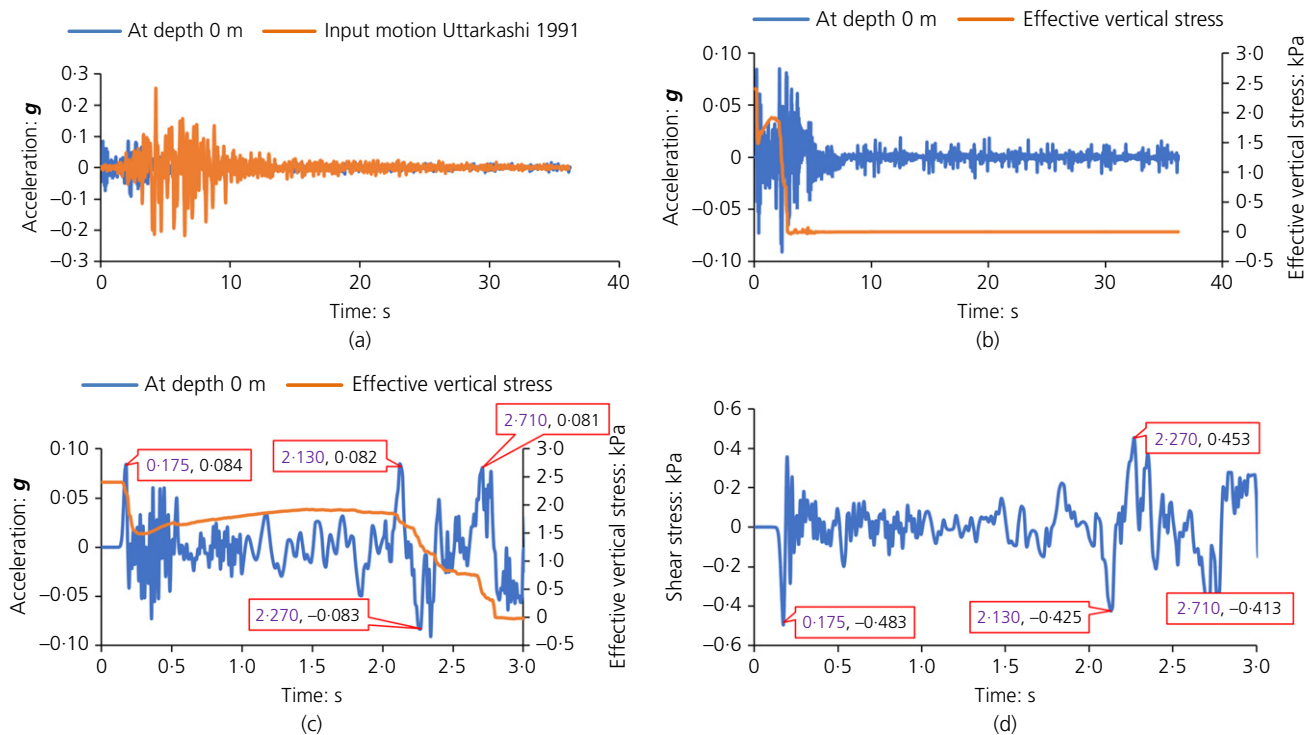
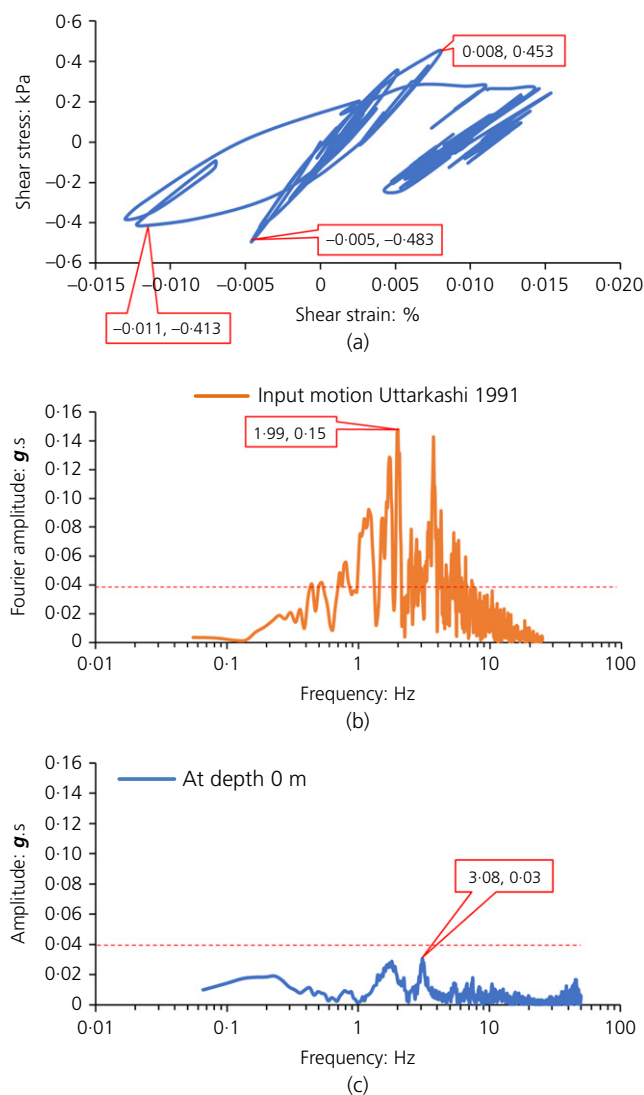


Fig. 12. (a) Acceleration records, (b) evolution of horizontal acceleration and effective vertical stress, (c) zoomed in view of the evolution of horizontal acceleration and effective vertical stress, (d) evolution of shear stress for the Uttarkashi earthquake (1991)



**Fig. 13.** (a) Shear stress–shear strain curve, (b) Fourier amplitude spectrum of input motion, (c) Fourier amplitude spectrum of horizontal acceleration obtained at the ground surface in the current analysis for the Uttarkashi earthquake (1991)

and 10(c), it is observed that the predominant frequency of the input motion is 1.7 Hz whereas that of the acceleration record at the ground surface is 2.07 Hz. From the Fourier spectrum plots, it is clear that due to liquefaction, most of the input frequency became deamplified. The magnitude scalogram for the Chamoli 1999 earthquake and the corresponding acceleration record at the ground surface are shown in Figs. 11(a) and 11(b), respectively. It is observed that a significant part of the input energy lies between 4 and 5.6 s, with a frequency spanning from 1.70 to 3.40 Hz. From Fig. 11(b), it is observed that the frequency of the acceleration spikes at 2.33 and 2.46 s is around 35.0 Hz. For input motion, frequency components above 10 Hz are almost absent over the entire motion, whereas for the acceleration record at the ground surface, frequency components above 10 Hz are present up to 5 s.

Acceleration and effective stress evolution plots for the Uttarkashi 1991 earthquake are shown in Fig. 12. From this figure, it is observed that a sudden reduction in the effective stress gives rise to acceleration spikes. From Figs. 12(c), 12(d) and 13(a), it is observed that the acceleration spikes correspond to the tip of the shear stress–shear strain curve. From the Fourier amplitude spectrum shown in Figs. 13(b)

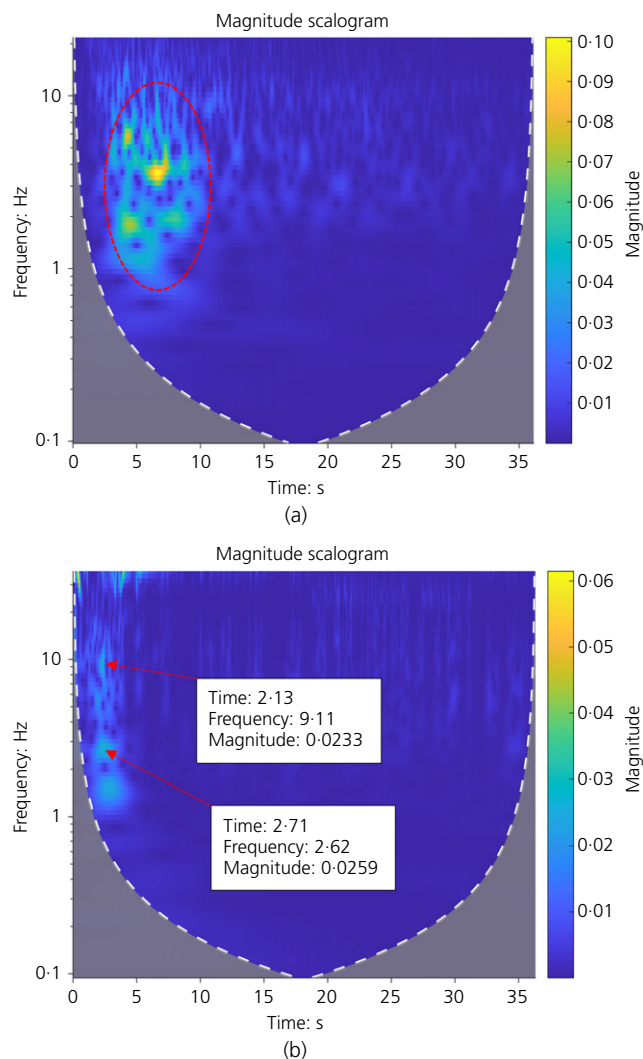


**Fig. 14.** Magnitude scalogram of the wavelet transform for (a) input motion Uttarkashi 1991 (b) of horizontal acceleration obtained at the ground surface in the current analysis for input motion Uttarkashi 1991

and 13(c), it is clear that due to liquefaction, most of the input frequency became deamplified. Furthermore, the predominant frequency of the input motion is 1.99 Hz, whereas that of the acceleration record at the ground surface is 3.08 Hz. From the magnitude scalogram of Uttarkashi 1991 motion shown in Fig. 14(a), it is observed that most of the energy of the input signal is concentrated below 10 s. From the scalogram of the acceleration record at the ground surface, shown in Fig. 14(b), it is observed that the frequency of the spikes at 2.13 and 2.71 s is 9.11 and 2.62 Hz, respectively.

## CONCLUSIONS

Site response analysis has been carried out for Bhuj (2001), Chamoli (1999) and Uttarkashi (1991) earthquakes having a predominant frequency of 1.2, 1.7 and 1.99 Hz, respectively. From the analysis, it is revealed that a sudden reduction in the effective stress results in a corresponding spike in the acceleration–time record. Moreover, this spike in the acceleration is observed to belong to the tip of the shear stress–shear strain curve. In the case of Bhuj (2001) earthquake, most of the frequency components below 10 Hz became deamplified, whereas amplification of the components

above 30 Hz is observed. In the case of Chamoli (1999) and Uttarkashi (1991) earthquakes, deamplification of the frequency components is observed over the almost entire duration. In all three cases, the predominant frequency of the acceleration record at the ground surface is observed to be greater than that of input motion. The magnitude scalogram of the wavelet transform helped understanding the distribution of the frequency components with time. From the magnitude scalograms, it is observed that the frequency of the acceleration spikes is greater than the predominant frequency of the acceleration record at the ground surface. Post-liquefaction, most of the significant input acceleration became deamplified.

Conventionally, a stress-based approach is most widely used to evaluate the liquefaction potential of the ground. In this approach, cyclic shear stress ratio is compared with cyclic resistance ratio. The cyclic shear stresses induced by earthquakes are obtained from: (1) site response analysis assuming the stress-strain response of the soil to be linear or equivalently linear or (2) a simplified procedure. This approach provides the factor of safety against liquefaction. However, it fails to provide any information regarding the effect of liquefaction on the acceleration and frequency content of the motion. Wavelet transforms coupled with Fourier transform and acceleration record provide details about the acceleration and frequency evolution over pre-and post-liquefaction shaking. It should be noted that wavelet transforms have a good frequency and poor time resolution at low frequencies and a good time and poor frequency resolution at high frequencies.

#### ACKNOWLEDGEMENTS

The first author is grateful to Mr. Rizwan Khan, a Research Scholar at the Indian Institute of Science, Bangalore, while interacting with whom the author came to know about wavelet transform. The constructive comments by the anonymous reviewers are gratefully acknowledged.

#### REFERENCES

- Anbazhagan, P., Uday, A., Moustafa, S. S. R. & Al-Arifí, N. S. N. (2016). Correlation of densities with shear wave velocities and SPT N values. *J. Geophys. Engng* **13**, No. 3, 320–341, <https://doi.org/10.1088/1742-2132/13/3/320>.
- Baker, J. W. (2007). Quantitative classification of near-fault ground motions using wavelet analysis. *Bull. Seismol. Soc. Am.* **97**, No. 5, 1486–1501, <https://doi.org/10.1785/0120060255>.
- Bolton, M. D. (1986). The strength and dilatancy of sands. *Géotechnique* **36**, No. 1, 65–78, <https://doi.org/10.1680/geot.1986.36.1.65>.
- Bonal, J., Donohue, S. & McNally, C. (2012). Wavelet analysis of bender element signals. *Géotechnique* **62**, No. 3, 243–252, <https://doi.org/10.1680/geot.9.P052>.
- Chakraborty, A. & Okaya, D. (1995). Frequency–time decomposition of seismic data using wavelet-based methods. *Geophysics* **60**, No. 6, 1906–1916, <https://doi.org/10.1190/1.1443922>.
- Chatterjee, P. (2015). *Wavelet analysis in civil engineering*. Boca Raton, FL, USA: CRC Press, Taylor & Francis Group, <https://doi.org/10.1201/b18057>.
- Chavan, D. (2021). *Liquefaction resistance and cyclic response of air – injected desaturated clean sandy soil: experimental and numerical investigations*. Bangalore, India: Indian Institute of Science, Bangalore. See <https://etd.iisc.ac.in/handle/2005/5226>.
- Elgamal, A., Yang, Z. & Parra, E. (2002). Computational modeling of cyclic mobility and post liquefaction site response. *Soil Dyn. Earthq. Engng* **22**, No. 4, 259–271.
- Elgamal, A., Yang, Z. & Parra, E. (2003). Modeling of cyclic mobility in saturated cohesionless soils. *Int. J. Plast.* **19**, 883–905.
- Gang, W., Xing, W. & Zhao, J. (2018). Modelling spiky acceleration response of dilative sand deposits during earthquakes with emphasis on large post-liquefaction deformation. *Earthq. Engng Engng Vib.* **17**, No. 1, 125–138, <https://doi.org/10.1007/s11803-018-0429-x>.
- Idriss, I. M. & Boulanger, R. (2008). *Soil liquefaction during earthquakes*. Oakland, CA, USA: EERI.
- Ishihara, K. (1993). Liquefaction and flow failure during earthquakes. *Géotechnique* **43**, No. 3, 351–415, <https://doi.org/10.1680/geot.1993.43.3.351>.
- Ishihara, K. (1996). *Soil behaviour in earthquake geotechnics*. Oxford, UK: Oxford Science Publications.
- Javdanian, H., Heidari, A. & Raeisi, J. (2021). Seismic ground response under wavelet-based decomposed earthquake records. *Soil Dyn. Earthq. Engng* **149**, No. June, 1–11, <https://doi.org/10.1016/j.soildyn.2021.106865>.
- Joyner, W. B. & Chen, A. T. F. (1975). Calculation of nonlinear ground response in earthquakes. *Bull. Seismol. Soc. Am.* **65**, No. 5, 1315–1336, <http://www.bssaonline.org/content/65/5/1315.abstract>.
- Kamgar, R., Tavakoli, R., Rahgozar, P. & Jankowski, R. (2021). Application of discrete wavelet transform in seismic nonlinear analysis of soil–structure interaction problems. *Earthq. Spectra* **37**, No. 3, <https://doi.org/10.1177/8755293020988027>.
- Kokusho, T. (2014). Seismic base-isolation mechanism in liquefied sand in terms of energy. *Soil Dyn. Earthq. Engng* **63**, 92–97, <https://doi.org/10.1016/j.soildyn.2014.03.015>.
- Kramer, S. L. (1996). *Geotechnical earthquake engineering*. Delhi, India: Pearson.
- Kuhlemeyer, R. L. & Lysmer, J. (1973). Finite element method accuracy for wave propagation problems. *J. Soil Mech. Found. Div.* **99**, No. 5, <https://doi.org/10.1061/JSFEAQ.0001885>.
- MathWorks (2020). *Matlab (R2020a)*. Natick, MA, USA: The MathWorks, Inc.
- MathWorks (2021). *Continuous wavelet transform and scale-based analysis*. Natick, MA, USA: The MathWorks, Inc. See <https://in.mathworks.com/help/wavelet/gs/continuous-wavelet-transform-and-scale-based-analysis.html> (accessed 10/10/2021).
- Mazzoni, S., McKenna, F., Scott, M. H. & Fenves, G. L. (2007). *OpenSees Command Language Manual*.
- Pietruszczak, S., Pande, G. N. & Oulapour, M. (2003). A hypothesis for mitigation of risk of liquefaction. *Géotechnique* **53**, No. 9, 833–838, <https://doi.org/10.1680/geot.2003.53.9.833>.
- Polikar, R. (1996). *The wavelet tutorial*, 2nd edn.
- Seed, H. B. & Idriss, I. M. (1970). Soil moduli and damping factors for dynamic analysis. *Earthq. Engng Res. Center* No. 70–10, 41.
- Todorovska, M. I., Meidani, H. & Trifunac, M. D. (2009). Wavelet approximation of earthquake strong ground motion-goodness of fit for a database in terms of predicting nonlinear structural response. *Soil Dyn. Earthq. Engng* **29**, No. 4, 742–751, <https://doi.org/10.1016/j.soildyn.2008.08.001>.
- Veeraraghavan, S., Spears, R. E. & Coleman, J. L. (2019). High frequency content in nonlinear soil response: a numerical artifact or a reality? *Soil Dyn. Earthq. Engng* **116**, No. June 2017, 185–191, <https://doi.org/10.1016/j.soildyn.2018.09.044>.
- Yang, Z. (2000). *Numerical modeling of earthquake site response including dilation and liquefaction*. New York, NY, USA: Columbia University.
- Zeghal, M. & Elgamal, A. W. (1994). Analysis of site liquefaction using earthquake records. *J. Geotech. Engng* **120**, No. 6, 996–1017, [https://doi.org/10.1061/\(ASCE\)0733-9410\(1994\)120:6\(996\)](https://doi.org/10.1061/(ASCE)0733-9410(1994)120:6(996)).

#### HOW CAN YOU CONTRIBUTE?

To discuss this paper, please submit up to 500 words to the editor at [journals@ice.org.uk](mailto:journals@ice.org.uk). Your contribution will be forwarded to the author(s) for a reply and, if considered appropriate by the editorial board, it will be published as a discussion in a future issue of the journal.